












# The rare X-ray flaring activity of the ultraluminous X-ray source NGC 4559 X7

Fabio Pintore <sup>1,2</sup>★, S. Motta <sup>3</sup>, C. Pinto <sup>2</sup>, M. G. Bernardini <sup>3</sup>, G. Rodriguez-Castillo <sup>1,2,4</sup>, R. Salvaterra <sup>1</sup>, G. L. Israel <sup>4</sup>, P. Esposito <sup>5</sup>, E. Ambrosi <sup>2</sup>, C. Salvaggio <sup>3,6</sup>, L. Zampieri <sup>7</sup> and A. Wolter <sup>3</sup>

<sup>1</sup>INAF – IASF Milano, Via E. Bassini 15, I-20133 Milano, Italy

<sup>2</sup>INAF – IASF Palermo, Via U. La Malfa 153, I-90146 Palermo, Italy

<sup>3</sup>INAF – Osservatorio Astronomico di Brera, via Brera 28, I-20121 Milano, Italy

<sup>4</sup>INAF – Osservatorio astronomico di Roma, Via Frascati 44, I-00040 Monteporzio Catone, Italy

<sup>5</sup>Scuola Universitaria Superiore IUSS Pavia, Piazza della Vittoria 15, I-27100 Pavia, Italy

<sup>6</sup>Dipartimento di Fisica, Università degli Studi di Milano-Bicocca, Piazza della Scienza 3, I-20126 Milano, Italy

<sup>7</sup>INAF – Osservatorio Astronomico di Padova, Vicolo dell'Osservatorio 5, I-35122 Padova, Italy

Accepted 2021 March 26. Received 2021 March 15; in original form 2021 February 2

## ABSTRACT

Ultraluminous X-ray sources are considered amongst the most extremely accreting objects in the local Universe. The recent discoveries of pulsating neutron stars in ULXs strengthened the scenario of highly super-Eddington accretion mechanisms on stellar mass compact objects. In this work, we present the first long-term light curve of the source NGC 4559 X7 using all the available *Swift/XRT*, *XMM–Newton*, *Chandra*, and *NuSTAR* data. Because of the high quality 2019 *XMM–Newton* and *NuSTAR* observations, we investigated in an unprecedented way the spectral and temporal properties of NGC 4559 X7. The source displayed flux variations of up to an order of magnitude and an unusual flaring activity. We modelled the spectra from NGC 4559 X7 with a combination of two thermal components, testing also the addition of a further high energy cut-off power law. We observed a spectral hardening associated with a luminosity increase during the flares, and a spectral softening in the epochs far from the flares. Narrow absorption and emission lines were also found in the RGS spectra, suggesting the presence of an outflow. Furthermore, we measured hard and (weak) soft lags with magnitudes of a few hundreds of seconds whose origin is possibly due to the accretion flow. We interpret the source properties in terms of a super-Eddington accretion scenario assuming the compact object is either a light stellar mass black hole or a neutron star.

**Key words:** accretion, accretion discs – X-rays: binaries – X-Rays: galaxies – X-rays: individual: NGC 4559 X7.

## 1 INTRODUCTION

Ultraluminous X-ray sources (ULX) are a class of non-nuclear accreting compact objects displaying X-ray luminosities higher than  $10^{39}$  erg s<sup>−1</sup> and up to  $10^{41 \div 42}$  erg s<sup>−1</sup> (e.g. Kaaret, Feng & Roberts 2017). The nature of the compact object, in the vast majority of ULXs, is nowadays believed to be of stellar type, i.e. stellar mass black holes (BHs;  $M_{\text{BH}} = 5\text{--}80 M_{\odot}$ ) or neutron stars (NSs). In particular, six exaccreting ULXs hosting pulsating NSs (PULXs), with spin periods in the range 0.5–20 s have been discovered in recent years (Bachetti et al. 2014; Israel et al. 2017; Israel et al. 2017; Carpano et al. 2018; Rodríguez Castillo et al. 2020; Sathyaprakash et al. 2019), suggesting that the NS population in ULXs can be larger than previously expected (see e.g. Middleton & King 2017; Koliopanos et al. 2017; Pintore et al. 2017; Walton et al. 2018; King & Lasota 2020). It is believed that, because of the transient behaviour of the observed pulsations in PULXs, many NSs in ULXs can remain undetected and can be unveiled only through indirect evidences as, for instance, the presence of cyclotron absorption lines (as in the case

of M51 ULX-8; Brightman et al. 2018; Middleton et al. 2019) or a flux switch-off due to propeller phase (e.g. Tsygankov et al. 2016; Earnshaw, Roberts & Sathyaprakash 2018). A further indication of an NS accretor may be the presence of a hard spectrum, a common characteristic of all PULXs, and which may be associated with an accretion column above the NS surface (e.g. Pintore et al. 2017; Walton et al. 2018, 2020).

The assumption that the accretor is a stellar mass compact object implies super-Eddington accretion, where a certain degree of geometrical beaming may be taken into account to explain the observed high X-ray luminosity in ULXs. Magneto-hydrodynamical simulations showed that, in case of super-Eddington accretion, strong optically thick outflows in the form of winds can be radiatively ejected by the accretion disc (e.g. Poutanen et al. 2007; Ohsuga & Mineshige 2011; Takeuchi, Ohsuga & Mineshige 2014), from radii smaller than the so-called spherization radius ( $R_{\text{sph}} \propto \dot{m}_0$ , where  $\dot{m}_0$  is the accretion rate in Eddington rate unit; e.g. Poutanen et al. 2007). Observational evidence in favour of powerful outflows/winds were identified in some ULXs in which blue-shifted ( $z \sim 0.2c$ ) absorption lines have been detected (e.g. Pinto, Middleton & Fabian 2016; Pinto et al. 2017; Kosec et al. 2018). In addition, such winds are believed to be the main cause of the time lags between soft and hard X-ray

\* E-mail: [fabio.pintore@inaf.it](mailto:fabio.pintore@inaf.it)

photons observed in some ULXs, such as NGC 55 ULX-1 (Pinto et al. 2017), NGC 5408 X-1 (e.g. Heil & Vaughan 2010; De Marco et al. 2013), and NGC 1313 X-1 (Kara et al. 2020). Such lags, conventionally labelled as negative lags (or soft lags, because the soft photons lag the hard ones), are observed at low frequencies ( $\sim 0.1$ – $10$  mHz) with a magnitude of tens to thousands of seconds, and are thought to originate from the propagation of hard photons through a very extended optically thick medium, likely associated with the base of the outflows. Because of the generally low ULX count-rate, time lags appear to be preferentially observed in sources with high short-term variability. The presence of flaring activity was also observed in epochs where lags were found, as in the case of the ULX NGC 1313 X-1 (Kara et al. 2020). However, flares as well as heart-beat variability are not so common in ULXs and only a handful of sources showed them (e.g. NGC 7456 ULX-1, Pintore et al. 2020; NGC 253 ULX-1, Barnard 2010; NGC 6946 ULX-3, Earnshaw et al. 2019; NGC 247 ULX-1, Pinto et al., in preparation; 4XMM J111816.0-324910 in NGC 3621, Motta et al. 2020).

In this work, we report on the source NGC 4559 X7 (also known as RX J123551+27561; X7 hereafter), a ULX in the galaxy NGC 4559, which showed a peculiar flaring activity during X-ray observations taken with *XMM-Newton* and *NuSTAR* in 2019. NGC 4559 is a spiral galaxy historically assumed to be at a distance of  $\sim 10$  Mpc (Tully & Fisher 1988; Sanders et al. 2003; although the lower distance limit is  $\sim 7$  Mpc, Sorce et al. 2014). The galaxy hosts two ULXs (X7 and X10; e.g. Soria et al. 2004) that have been poorly studied in the past. Only a few short *Chandra* and *XMM-Newton* observations of NGC 4559 are available in the archives, during which the two ULXs showed extremely high 0.3–10 keV luminosity ( $> 10^{40}$  erg s $^{-1}$ ), if a distance to the source of 10 Mpc is assumed. X7 lies in the outskirts of the galaxy (RA = 12<sup>h</sup> 35<sup>m</sup> 51<sup>s</sup>.71, Dec. = +27<sup>d</sup> 56<sup>m</sup> 04<sup>s</sup>.1; Swartz et al. 2011), inside a region rich of OB-type stars with low metallicity ( $0.2 < Z/Z_{\odot} < 0.4$ ), where Soria et al. (2004) identified its possible optical counterpart as a blue supergiant of 20 M $_{\odot}$  and an age of  $\sim 10$  Myr.

## 2 DATA REDUCTION

### 2.1 *XMM-Newton*

*XMM-Newton* observed NGC 4559 on 2003 May 27 for  $\sim 42$  ks. Then, our group obtained a new  $\sim 75$  ks long observation, which was taken on 2019 June 16 (PI: F. Pintore; Table 1). We reduced the two observations with SAS v18.0.0. We used data from both EPIC-pn and EPIC-MOS (1 and 2) cameras: events were selected considering PATTERN  $\leq 4$  (i.e. single and double-pixel events) for the PN, and PATTERN  $\leq 12$  (i.e. single- and multiple-pixel events) for the MOS. We extracted source and background events from circular regions with radii of 30 and 60 arcsec, respectively. The photon times of arrival were converted to the barycenter of the Solar System with the task BARYCEN, using the best *Chandra* coordinates (RA = 12<sup>h</sup> 35<sup>m</sup> 51<sup>s</sup>.71, Dec. = +27<sup>d</sup> 56<sup>m</sup> 04<sup>s</sup>.1; Swartz et al. 2011) of the target.

Both observations were only marginally affected by high background epochs, which were excluded from the analysis. This resulted in a net exposure time of  $\sim 35$  and  $\sim 65$  ks for the observations taken in 2003 and 2019, respectively. Source and background spectra were grouped, with the FTOOLS *grppha*, in order to accumulate at least 25 counts per energy bin, and we applied the SAS task EPICLCCORR to all light curves.

We also used data from the reflection grating spectrometer (RGS; den Herder et al. 2001) of the 2019 observation, where X7 was at the centre of the field of view. The RGS data were reduced

with the RGSPROC task, which produces calibrated event files, spectra, response matrices, and 1D images. Following the standard procedures, we filtered the RGS data for solar flares using the background light curve from the RGS CCD number 9 (corresponding to  $\lesssim 7.5$  Å or  $\gtrsim 1.7$  keV). The background light curves were binned at a 100 s time resolution and all the time bins with a count rate above 0.2 cts s $^{-1}$  were rejected. We used the same GTI for both the RGS 1 and 2, and obtained an exposure time of 71.2 ks for each detector. The net exposure time is slightly longer than the EPIC one owing to the lower RGS background contamination.

### 2.2 *NUSTAR*

The *NuSTAR* observation (Obs.ID: 30501004002) was taken about 6.4 h after the 2019 *XMM-Newton* observation (Table 1). The total exposure time of this observation is  $\sim 95$  ks. We processed and reduced the data with the standard NUPIPELINE task of the *NuSTAR Data Analysis Software* v1.3.0 (NUSTARDAS) in the HEASOFT package version 6.25, adopting standard filtering and corrections. Spectra were extracted from circular regions with radius 60 arcsec for both source and background. Spectra were then rebinned to accumulate at least 25 counts per energy bin.

### 2.3 *Chandra*

We analysed the *Chandra* observations of 2001 January 14 and June 4, and 2002 March 14, with exposures of 9.7, 11, and 3 ks, respectively (Table 1). We reduced the data with CIAO v4.9 and calibration CALDB v4.7.6. We selected source and background events from circular regions with radii 3 and 15 arcsec, respectively. The source spectra were obtained with the task SPECEXTRACT of the CIAO package, which produces appropriate response and auxiliary files.

Source and background spectra were grouped with *grppha* in order to accumulate at least 25 counts per energy bin.

### 2.4 *Swift*

The *Neil Gehrels Swift Observatory* (hereafter *Swift*) observed the galaxy NGC 4559 for 56 times between 2006 January and 2021 March (Table 1). Most observations were taken in PC mode with an average exposure time of about 1–2 ks each. We reduced the data with the XRTPIPELINE tool, and we extracted source and background events from circular regions of radii 40 and 60 arcsec (centred at the source position and in a source-free region of the CCD), respectively. We used the *Swift/XRT* observations only to construct a long-term light curve, as the data quality is not good enough to allow us to perform high quality spectral analysis of individual or stacked pointing. We estimated the source flux in each observation by fitting an absorbed power-law model with photon index and column density fixed at 2 and  $1.5 \times 10^{21}$  cm $^{-2}$ , respectively, and letting only the power-law normalization to vary. The choice of this reference model was adopted because of the poor quality of the spectra.

## 3 LONG- AND SHORT-TERM VARIABILITY

The long-term X-ray light curve shows that X7 varies in flux by up to a factor of  $\sim 5$ – $6$ . The observed source flux peaked during the 2019 *XMM-Newton* observation of our X-ray campaign. *Swift/XRT* and *NuSTAR* pointed at X7 a few hours later, finding the source at a mean flux a factor of  $\sim 3$  lower than during the *XMM-Newton* observation.

**Table 1.** Log of the observations used in this work.

	Instr.	Obs.ID	Start [YYYY-MM-DD hh:mm:ss (TT)]	Stop	Exp. (ks)
1	<i>Chandra</i>	2026	2001-01-14T16:24:39	2001-01-14T19:27:35	9.4
2	<i>Chandra</i>	2027	2001-06-04T01:14:29	2001-06-04T04:43:23	10.7
3	<i>Chandra</i>	2686	2002-03-14T05:13:59	2002-03-14T06:34:19	3.0
4	<i>XMM-Newton</i>	0152170501	2003-05-27T03:07:30	2003-05-27T14:19:33	42.2
5	<i>Swift/XRT</i>	00032249001	2012-01-14T15:53:31	2012-01-14T20:41:16	3.9
6	<i>Swift/XRT</i>	00032249003	2012-01-16T01:01:11	2012-01-16T06:17:57	4.2
7	<i>Swift/XRT</i>	00032249004	2012-01-18T01:33:23	2012-01-18T19:21:55	3.1
8	<i>Swift/XRT</i>	00032249005	2012-01-20T04:35:58	2012-01-20T12:58:55	3.8
9	<i>Swift/XRT</i>	00576064000	2013-10-28T05:46:26	2013-10-28T07:38:28	3.5
10	<i>Swift/XRT</i>	00032249006	2014-02-27T18:39:59	2014-03-03T11:21:54	4.9
11	<i>Swift/XRT</i>	00032249007	2014-03-05T23:46:07	2014-03-05T23:59:55	0.8
12	<i>XMM-Newton</i>	0842340201	2019-06-16T19:03:44	2019-06-17T15:06:27	74.3
13	<i>Swift/XRT</i>	00088825001	2019-06-17T22:40:58	2019-06-17T23:08:53	1.7
14	<i>NuSTAR</i>	30501004002	2019-06-17T21:31:09	2019-06-20T04:01:09	94.9
15	<i>Swift/XRT</i>	00032249008	2019-12-12T00:46:13	2019-12-12T01:09:52	1.4
16	<i>Swift/XRT</i>	00032249009	2019-12-19T12:50:14	2019-12-19T13:12:53	1.4
17	<i>Swift/XRT</i>	00032249011	2020-01-02T08:32:43	2020-01-02T08:47:53	0.9
18	<i>Swift/XRT</i>	00032249012	2020-01-09T06:04:44	2020-01-09T06:21:52	1.0
19	<i>Swift/XRT</i>	00032249013	2020-01-16T00:40:59	2020-01-16T00:50:53	0.6
20	<i>Swift/XRT</i>	00032249014	2020-01-23T15:43:19	2020-01-23T16:05:53	1.3
21	<i>Swift/XRT</i>	00032249015	2020-01-30T16:42:51	2020-01-30T17:04:52	1.3
22	<i>Swift/XRT</i>	00032249016	2020-02-06T12:51:41	2020-02-06T13:14:53	1.4
23	<i>Swift/XRT</i>	00032249017	2020-02-13T13:49:35	2020-02-13T14:08:54	1.2
24	<i>Swift/XRT</i>	00032249018	2020-02-20T00:24:36	2020-02-20T02:08:52	1.4
25	<i>Swift/XRT</i>	00032249019	2020-02-27T12:21:16	2020-02-27T12:43:52	1.4
26	<i>Swift/XRT</i>	00032249020	2020-03-05T11:39:38	2020-03-05T12:01:52	1.3
27	<i>Swift/XRT</i>	00032249021	2020-03-12T00:06:31	2020-03-12T00:26:52	1.2
28	<i>Swift/XRT</i>	00032249022	2020-03-19T10:17:34	2020-03-19T10:40:54	1.4
29	<i>Swift/XRT</i>	00032249023	2020-03-26T12:51:57	2020-03-26T13:14:54	1.4
30	<i>Swift/XRT</i>	00032249024	2020-04-02T12:11:47	2020-04-02T12:33:54	1.3
31	<i>Swift/XRT</i>	00032249025	2020-04-09T11:36:37	2020-04-09T11:53:52	1.0
32	<i>Swift/XRT</i>	00032249026	2020-04-16T07:50:00	2020-04-16T08:10:54	1.2
33	<i>Swift/XRT</i>	00032249027	2020-04-23T02:09:17	2020-04-23T02:32:54	1.4
34	<i>Swift/XRT</i>	00032249028	2020-04-30T11:11:28	2020-04-30T11:33:52	1.3
35	<i>Swift/XRT</i>	00032249029	2020-05-07T12:05:07	2020-05-07T12:28:54	1.4
36	<i>Swift/XRT</i>	00032249030	2020-05-14T11:29:05	2020-05-14T11:45:53	1.0
37	<i>Swift/XRT</i>	00032249031	2020-05-21T12:24:35	2020-05-21T12:42:53	1.1
38	<i>Swift/XRT</i>	00035479001	2006-01-02T18:56:44	2006-01-03T04:47:56	5.3
39	<i>Swift/XRT</i>	00032249032	2020-05-28T11:29:03	2020-05-28T11:51:52	1.4
40	<i>Swift/XRT</i>	00032249033	2020-06-04T07:44:35	2020-06-04T08:11:53	1.6
41	<i>Swift/XRT</i>	00032249034	2020-06-11T07:06:17	2020-06-11T07:28:53	1.4
42	<i>Swift/XRT</i>	00032249035	2020-06-18T04:46:38	2020-06-18T05:09:52	1.4
43	<i>Swift/XRT</i>	00032249036	2020-06-25T07:14:56	2020-06-25T07:38:53	1.4
44	<i>Swift/XRT</i>	00032249037	2020-07-02T05:00:02	2020-07-02T05:20:53	1.2
45	<i>Swift/XRT</i>	00032249038	2020-07-09T01:00:01	2020-07-09T01:23:53	1.4
46	<i>Swift/XRT</i>	00032249039	2020-07-16T03:41:41	2020-07-16T04:00:52	1.1
47	<i>Swift/XRT</i>	00032249040	2020-07-23T20:20:22	2020-07-23T20:46:51	1.6
48	<i>Swift/XRT</i>	00032249041	2020-07-30T07:01:53	2020-07-30T07:25:55	1.4
49	<i>Swift/XRT</i>	00032249042	2020-08-06T12:36:18	2020-08-06T13:01:52	1.5
50	<i>Swift/XRT</i>	00032249043	2020-10-28T13:48:32	2020-10-28T14:12:52	1.5
51	<i>Swift/XRT</i>	00032249044	2020-11-04T16:15:16	2020-11-04T16:37:53	1.4
52	<i>Swift/XRT</i>	00032249045	2020-11-11T05:57:36	2020-11-11T17:30:53	1.5
53	<i>Swift/XRT</i>	00032249046	2020-11-18T03:39:42	2020-11-18T04:01:53	1.3
54	<i>Swift/XRT</i>	00032249047	2020-11-25T06:09:00	2020-11-25T06:33:52	1.5
55	<i>Swift/XRT</i>	00032249048	2021-01-24T17:41:56	2021-01-24T18:09:53	1.7
56	<i>Swift/XRT</i>	00032249049	2021-01-31T09:03:13	2021-01-31T22:09:54	1.6
57	<i>Swift/XRT</i>	00032249050	2021-02-07T16:35:44	2021-02-07T16:44:54	0.5
58	<i>Swift/XRT</i>	00032249051	2021-02-14T15:27:42	2021-02-14T20:36:53	1.5
59	<i>Swift/XRT</i>	00032249052	2021-02-21T14:53:45	2021-02-21T22:52:53	1.6
60	<i>Swift/XRT</i>	00032249053	2021-02-28T04:44:06	2021-02-28T20:26:52	1.3
61	<i>Swift/XRT</i>	00032249054	2021-03-07T10:06:21	2021-03-07T13:53:52	0.5
62	<i>Swift/XRT</i>	00032249055	2021-03-14T11:03:30	2021-03-14T19:15:51	1.5

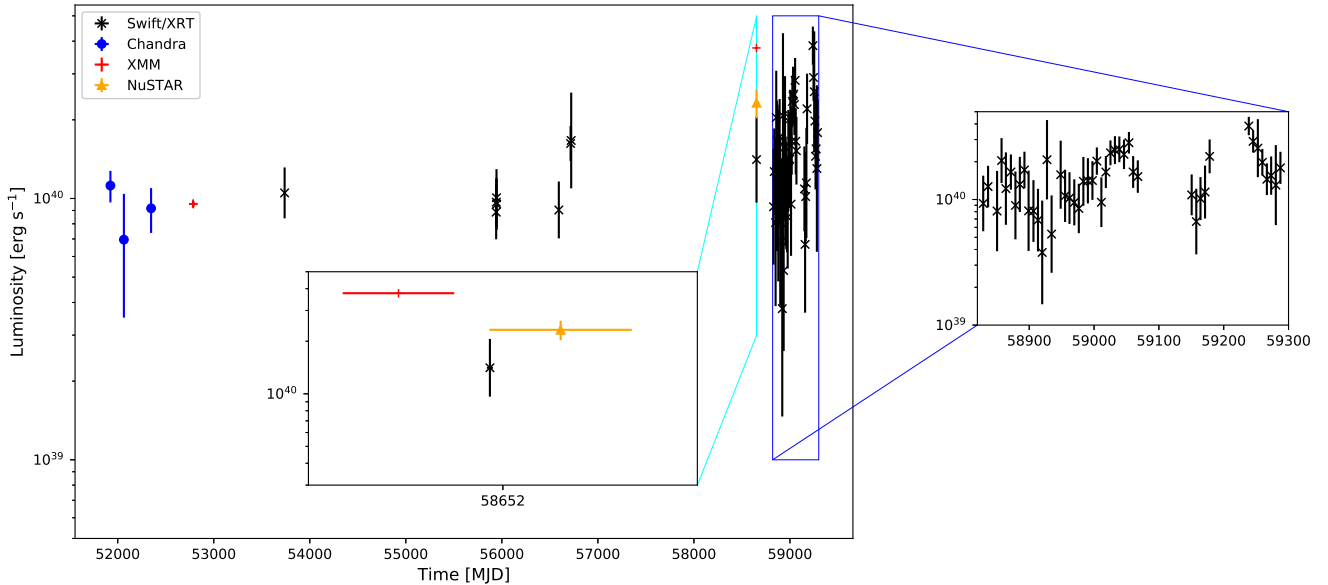


**Figure 1.** Long-term light curve of X7 in the 0.3–10 keV energy band obtained from the *XMM–Newton*, *NuSTAR*, *Chandra*, and *Swift/XRT* observations. The luminosities (not corrected for absorption) refer to the average values for all the observations and are calculated assuming a distance of 10 Mpc. The source luminosities in the *Swift/XRT* observations are estimated by adopting an absorbed power-law model (see text for details).

This indicates that flux variations in X7 may happen on a few hours time-scales (Fig. 1).

Remarkably, the 2019 *XMM–Newton* and *NuSTAR* observations caught a period of flaring activity of X7, never seen in any of the previous X-ray observations of the source. In particular, we found two flares in the *XMM–Newton* observation, at MJD  $\sim 58651.22$  and  $58651.33$ , and at least four (or possibly five) flares in the *NuSTAR* observation, at MJD  $\sim 58652.46$ ,  $58652.52$ ,  $58652.61$ , and  $58652.99$  (Fig. 2). Furthermore, in the last  $\sim 15$  ks of the *XMM–Newton* observation (i.e. from MJD 58651.44), we observed a high flux phase following the flares, which plateaued at a flux level compatible with that at the peak of the flares (see Fig. 2). During the high-flux phase, the source flux increased by more than a factor of  $\sim 4$  with respect to the persistent pre-flare emission, implying that the luminosity of X7 can vary by over almost an order of magnitude.

The flares show a variable duration of  $\sim 5$ – $10$  ks and, based on the *XMM–Newton* observation, their shape is mildly energy dependent (Fig. 2; we stacked the EPIC-pn and MOS1-2 cameras to obtain the light curve shown). The first flare in the *XMM–Newton* curve presents a double peak at energies  $< 2$  keV, but appears to be single peaked at higher energies. Despite the lower signal-to-noise ratio of the *NuSTAR* data, we note that in these data the flares seem to be grouped: at least three flares occurring in fast succession can be identified around MJD 58652.6, and two flares around MJD 58653. The limited count statistics of the data prevents us to perform a more in-depth analysis, although a visual inspection suggests that the flares do not show any obvious repeating pattern.

We also note the existence of ‘dip’-like events during the high flux epochs in the last 15 ks of the *XMM–Newton* observation. Such features last for  $\sim 1$  ks and resemble the dips seen in NGC 55 ULX-1 (Stobbart, Roberts & Warwick 2004), as they appear stronger at higher energies. Unfortunately, we cannot determine if they are really ULX-like dips or rather a storm of not resolved flares.

Finally, the *Swift/XRT* observations taken in 2020–2021 seems to show a possible (super)orbital variability of X7 (see zoom-in Fig. 1), which is even more evident in the 1.5–10 keV energy band.

We performed a Lomb–Scargle analysis on these data only (i.e. we excluded all the scanty observations taken prior to 2020), and we found a possible best period of  $\sim 190$  d. Unfortunately, the number of covered periods is still poor, which makes not possible yet to confirm robustly such a variability. Further continuous *Swift/XRT* monitoring are needed.

## 4 2019 XMM-NEWTON AND NUSTAR OBSERVATIONS

### 4.1 Timing

We created three light curves of X7 by combining events collected with all the EPIC cameras in the energy band 0.3–10 keV. Then, we binned the data with 140 s (Nyquist frequency  $N_y = 0.0071$  Hz). In order to reach the best possible frequency resolution ( $\delta\nu = 1/T \approx 3 \times 10^{-5}$  Hz), we calculated one single power density spectrum (PDS) from the entire light curve. The resulting PDS is shown in Fig. 3. The *XMM–Newton* PDS appears featureless, characterized by low amplitude red noise. A low-significance narrow feature appears at frequency  $\approx 10^{-4}$  Hz, which can be ascribed to the flares visible in the light curve. We investigate the presence of variability on shorter time-scales as well (from a few tens to a few hundreds seconds). The resulting PDS appears completely dominated by the instrumental noise, and no other feature is significantly detected above it.

We also produced an average PDS from the *NuSTAR* observation. A typical *NuSTAR* observation features a large number of data segments separated by orbital gaps, which prevent from exploring via Fourier analysis the presence of long-term variability on time-scales longer than the typical data segment ( $\sim 1000$  s). Furthermore, the count rate of X7 as seen by *NuSTAR* is low (between 0.05 and 0.25 counts  $s^{-1}$ ). Therefore, for both the FMPA and FMPB instruments on-board *NuSTAR*, we only explored the short time-scales by producing PDS over data stretches of variable length (between 130 and 1050 s), which we averaged into one final PDS to increase the signal-to-noise ratio. Similar to the *XMM–Newton*



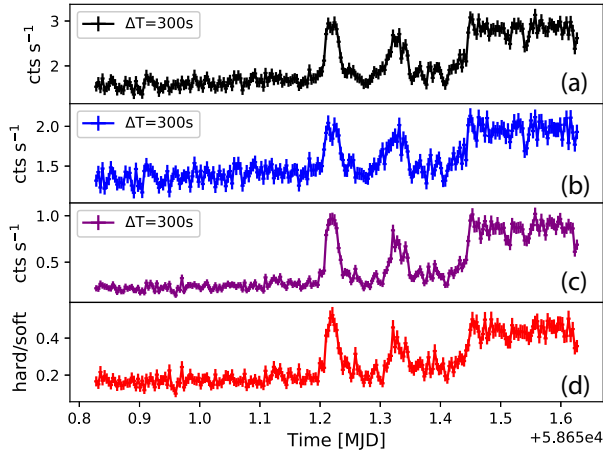


**Figure 2.** Left: EPIC-pn+MOS1/2 light-curves of X7 in the 0.3–10 keV (panel a), and 0.3–2.0 keV (panel b) and 2.0–10 keV (panel c), binned at 300 s. In panel (d), we also show the hardness ratio (hard band versus soft band) along the observation. There is a clear hardening of the source during the high flux epochs and the flares. Right: background-subtracted *NuSTAR*/FMPA+FMPB light curve binned at 500s. All the curves start on MJD 58650.

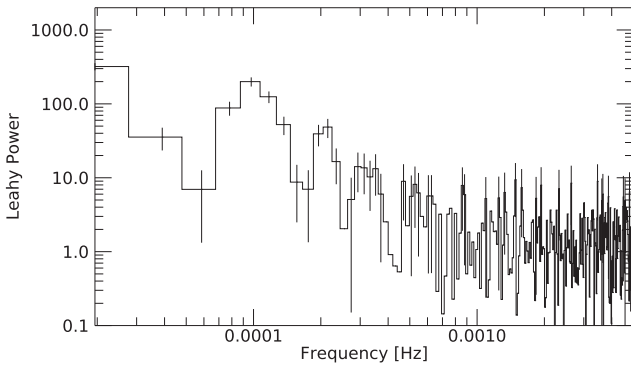
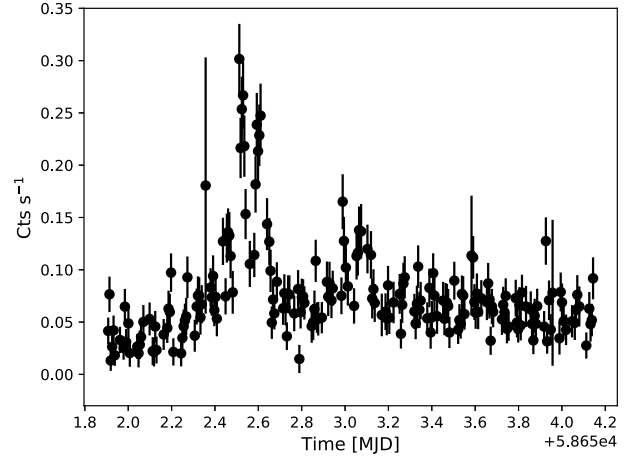


**Figure 3.** Power density spectrum calculated combining the data from all the *XMM-Newton* EPIC cameras.

case, the resulting PDS are dominated by instrumental noise, and no significant feature is detected.

#### 4.2 Search for pulsations

We searched for coherent signals in the 2019 *XMM-Newton*/EPIC-pn light curves of X7 in the 0.3–10 keV energy range (about 72 000 counts) by adopting the recipe outlined in Israel & Stella (1996). We first considered the effects of signal smearing introduced by the possible presence of a strong first period derivative component  $\dot{P}$ , as seen in many PULXs (see e.g. Israel et al. 2017). We corrected the photon arrival times by a factor  $-\frac{1}{2} \frac{\dot{P}}{P} t^2$  for a grid of about 2000 points in the range  $4 \times 10^{-6} < |\frac{\dot{P}}{P} (s^{-1})| < 5 \times 10^{-12}$  (see Rodríguez Castillo et al. 2020 for details). No significant peak was found and  $3\sigma$  upper limits to the pulsed fraction (PF), defined as the semi-amplitude of the sinusoid divided by the average count rate, were derived for the source. In the best cases, we obtained upper limits around 5–8 per cent in the 150 ms–150 s range. We then searched for pulsations applying orbital corrections for orbits with periods in the range  $\sim 2$  h–10 d, and composed by an NS and a companion star mass ranging from  $\sim 0.01$  up to  $100 M_{\odot}$ . No convincing pulsations were detected, but only a marginal detection of a signal at  $\sim 1.7$  s, with PF  $\sim 8$  per cent and significance  $\sim 3\sigma$ , for an orbital period of about 2.8 h and a companion star of mass  $\sim 0.2 M_{\odot}$ . However, we



note that such a companion mass value would be in contrast with the blue supergiant counterpart identified by Soria et al. (2004).

To investigate the 1.7 s candidate signal, we used its orbital parameters and all the available observations with enough statistics to reveal a  $\sim 8$  per cent PF signal. We searched in the 2003 *XMM-Newton* observation and in our *NuSTAR* (see Table 1) observation, which are the only two observations that could at least marginally detect such a low PF signal. We applied the corrections corresponding to the orbital parameters, but the 1.7 s signal candidate could not be confirmed. We may report on this candidate signal in future observations, with better counting statistics, which could allow us to convert its marginal significance to a robust detection.

#### 4.3 Time lags

The appearance of flaring activity in X7 prompted us to search for time lags between different energy bands, similar to those observed in the ULXs NGC 5408 X-1, NGC 55 ULX1, and NGC 1313 X-1 (De Marco et al. 2013; Pinto et al. 2017; Kara et al. 2020). We performed the analysis focusing only on the EPIC-pn data of the 2019 *XMM-Newton* observation to avoid stacking data from different instruments that may introduce fake variability. In order to do so, we created background-subtracted light curves in the 0.3–2 and 2–10 keV energy bands, where the source counting statistics are comparable.

We first performed a cross-correlation between the two light curves in the time domain using a non-mean subtracted discrete cross-correlation function (CCF; Band 1997). We used light curves binned to a time resolution of  $\Delta T = 20$  s (in order to exclude all the white noise at high frequencies) and choose the 2–10 keV range as reference energy band. We calculated the CCF value for a series of time delays  $k\Delta T$ , and we defined the lag as the time delay that corresponds to the global maximum of the circular CCF versus time delay, located by fitting an asymmetric Gaussian model to the CCF versus time delay. The uncertainties on the CCF have been derived by applying a flux-randomization method (Peterson et al. 1998). We found marginal indications of a positive lag (hard lag) of  $94 \pm 44$  s ( $1\sigma$  uncertainty), which, according to our convention, implies that the hard photons lag the soft photons.

We further investigated how the hard lag depends on the frequency. Following the recipe described in Uttley et al. (2014), we calculated the fast Fourier transform of the light curves in the 0.3–2 and

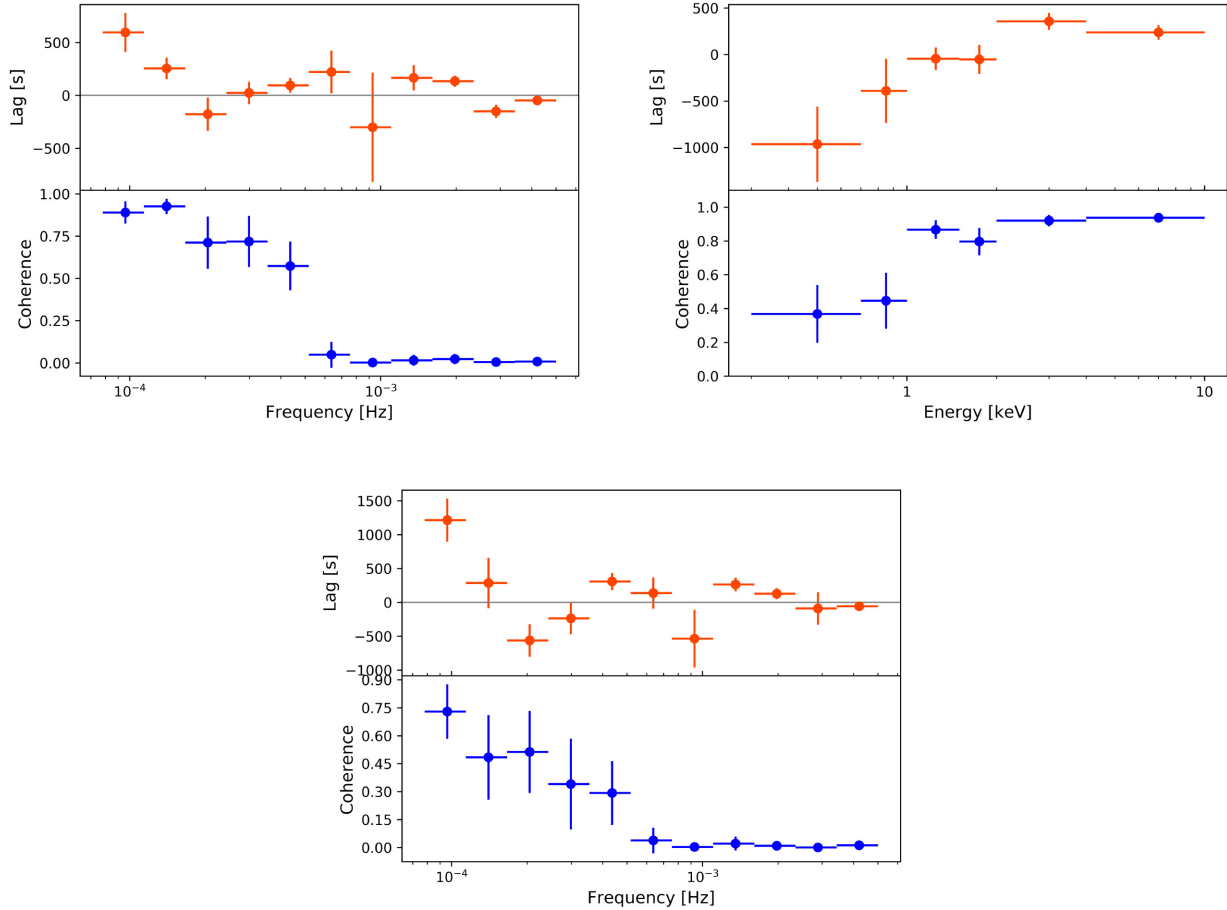


**Figure 4.** Time lag of X7 as a function of the frequency between the bands 0.3–2.0 and 2.0–10 keV (top left) and the lag spectrum in the  $(0.7–1.6) \times 10^{-4}$  Hz frequency range (top right). Bottom: lag versus frequency for the energy ranges 0.3–1.0 and 2.0–10 keV. According to the standard convention, positive lags imply the hard band lagging the soft band.

2–10 keV energy bands, binned with  $\Delta T = 100$  s, and we calculated the CCF. The latter was then averaged over five intervals, each of them containing segments of 128 time bins. Lags were then grouped in equally spatially logarithmic bins of frequency.

High coherence<sup>1</sup> between the two bands are observed for frequencies lower than  $\sim 10^{-3}$  Hz, while above this threshold the coherence dramatically drops to values consistent with zero (Fig. 4/top left). A hard lag in the frequency range  $(0.7–1.6) \times 10^{-4}$  Hz is seen, in a frequency region where the coherence is also high. The global significance of the lag (estimated by summing the significance of each lag point) in the  $(0.7–1.6) \times 10^{-4}$  Hz frequency range is higher than  $5\sigma$ . This result still confirms that, on long time-scales, the hard band lags the soft one for a weighted averaged value of  $335\text{s} \pm 89\text{s}$ , compatible within uncertainties with the value derived from the CCF. The frequency range at which the lag is found is compatible with the time interval between the two observed flares, which implies that the lag is likely mainly driven by such temporal features.

We verified the robustness of the positive time lag by performing a Monte Carlo simulation of 1000 light curves having the same variability observed in the EPIC-pn 0.3–10 keV energy band, rescaled to the mean count-rate found in the 0.3–2.0 and 2.0–10 keV bands.

<sup>1</sup> It is estimated, adopting the prescription of Uttley et al. (2014), as  $\gamma^2(v_j) = (|C_{XY}(v_j)|^2 - n^2) / (P_X(v_j) P_Y(v_j))$ , where  $C_{XY}(v_j)$  is the cross-spectrum at the  $j$ -frequency,  $n^2$  is the bias term, and  $P_{(X|Y)}$  are the PDS of the  $X$  and  $Y$  bands.

For each couple of simulated 0.3–2.0 and 2.0–10 keV light curves, we estimated the frequency-dependent lags and we inferred that a hard lag in the range  $(0.7–1.6) \times 10^{-4}$  Hz can be observed with a significance higher than  $5\sigma$  only three times over a total of 1000, i.e. a probability of 0.997 (hence  $\geq 3\sigma$ ), that the observed lags in the 2019 *XMM-Newton* observation are not due to chance coincidence.

We then extracted the lag-energy spectrum of the observed data in the frequency range  $(0.7–1.6) \times 10^{-4}$  Hz. For each energy bin, we calculated the lag using the 0.3–10 keV band as reference, from which we removed each band of interest. This is shown in Fig. 4/top right. The coherence clearly increases towards higher energies. At energies below 2 keV the lags are quite unconstrained although they suggest a soft lag, while above this energy the lags are significantly positive.

Besides the hard lag, we also note the hint ( $1\sigma$  significance) of a soft lag at frequencies around  $2 \times 10^{-4}$  Hz. However, when using the energy bands 0.3–1.0 and 2–10 keV, we found that the detection of the soft lag increases ( $\sim 2.5\sigma$  significance). The lag energy spectrum at these frequencies is shown in Fig. 4 (bottom panel).

#### 4.4 Spectral analysis

The hardness ratio between the energy bands 0.3–2.0 and 2.0–10 keV of the 2019 *XMM-Newton* observation clearly indicates a marked spectral variability along the observation, which in particular shows

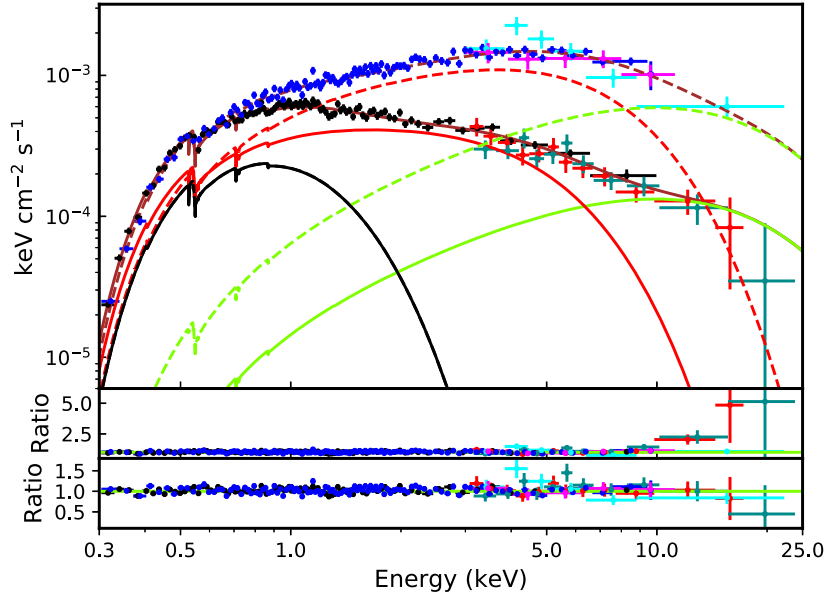


**Figure 5.** Unfolded *persistent* EPIC-pn (the black points) + *NuSTAR* A/B (the red and dark cyan points) spectrum, and *flare* EPIC-pn (the blue points) + *NuSTAR* A/B (the purple and cyan points) spectrum. The black, red, and green solid lines indicate the DISKBB, DISKPBB, and CUTOFFPL best-fitting models, respectively, for the *persistent* spectrum, while the brown solid line is the total model; we use the same colour coding for the dashed lines, which refer to best-fitting models of the *flare* spectrum. Middle panel: residuals of the fit with an absorbed DISKBB+DISKPBB model. Bottom panel: residuals of the best fit with an absorbed DISKBB+DISKPBB+CUTOFFPL model. Spectra have been rebinned for display purposes only.

evidence of a hardening during the flaring activity (Fig. 2; left, bottom panel). We investigated the spectral variability in both the *XMM-Newton* and *NuSTAR* 2019 observations, extracting a *persistent* and *flare* spectrum from both the *XMM-Newton* and the *NuSTAR* observations.

In *XMM*, the *persistent* spectrum was extracted over the first part of the observation, where no flares were detectable ( $\sim 28$  ks). The *flare* spectrum was extracted by considering only the times when the count rate was higher than  $1.1 \text{ cts s}^{-1}$  in the 0.3–10 keV EPIC-pn light curve, which resulted in a net exposure of 18 ks. In *NuSTAR*, we instead selected the *persistent* and *flare* epochs manually. The *flare* spectrum was extracted by choosing the latter as time intervals where the count rate was significantly higher than the average one. Even though we adopted a different approach for *XMM-Newton* and *NuSTAR*, we highlight that the *flare* and *persistent* spectra obtained with the two satellites are well comparable above 3 keV.

We simultaneously analysed the *XMM-Newton*+*NuSTAR* spectra of the two epochs in the range 0.3–30 keV, using XSPEC v.12.10.1. We adopted TBABS to model the absorption, assuming no variations of the absorption column density along the line of sight during the two epochs (i.e. we linked the parameter between the spectra). As typically found for ULXs, the X7 spectra cannot be described by simple models such as an absorbed single POWERLAW or a DISKBB ( $\chi^2_\nu > 3$ ). The data are well modelled by either a single Comptonization model (NTHCOMP in XSPEC, Zdziarski, Johnson & Magdziarz 1996;  $\chi^2_\nu = 0.97/1804$ ) or a combination of thermal models. A model in the form TBABS  $\times$  (DISKBB+DISKPBB<sup>2</sup>) provides a statistically acceptable fit, with ( $\chi^2_\nu = 0.99/1803$ ). Comparing the *flare* and *persistent* spectra, the low-energy DISKBB component is consistent with being constant within 90 per cent uncertainties

therefore we linked its temperature and normalization to a common value across the spectra.

Even though the resulting best fit is statistically acceptable ( $\chi^2_\nu = 0.99/1803$ ), we note the presence of a hard excess in the form of structured residuals above 10 keV (see Fig. 5, centre panel), as in many other PULXs and ULXs observed with *NuSTAR* (e.g. Bachetti et al. 2013; Walton et al. 2020). To take into account the high energy excess, we added a cut-off power-law component (CUTOFFPL in XSPEC), which has been found previously to be representative of the high-energy emission in PULXs. Such a component is usually interpreted as due to the presence of an accretion column above the NS, and it appears to be present also in ULXs where the nature of the compact object could not be determined yet (Walton et al. 2018). The simple inclusion of a cut-off power law to the best-fitting model causes a number of spectral parameters to become unconstrained. Hence, we fixed the spectral parameters of the cut-off power law to the average values found for the PULXs spectra, i.e.  $\Gamma = 0.59$  and  $E_{\text{cut}} = 7.1 \text{ keV}$ , and left only the model normalization amongst the spectra free to vary. The final model [TBABS (DISKBB+DISKPBB+CUTOFFPL)] provided a very good fit ( $\chi^2_\nu = 0.97/1801$ ; Fig. 5, top and bottom panel), which suggests that during the flaring activity both the DISKPBB and the CUTOFFPL contributed to the high-energy flux increase. All the results are reported in Table 2. The measured absorbed 0.3–30 keV fluxes are  $(2.08 \pm 0.03) \times 10^{-12}$  and  $(5.16 \pm 0.07) \times 10^{-12} \text{ erg cm}^2 \text{ s}^{-1}$  for the *persistent* and *flare* spectra, respectively, corresponding to luminosities of  $(2.48 \pm 0.04) \times 10^{40}$  and  $(6.15 \pm 0.09) \times 10^{40} \text{ erg s}^{-1}$  (for a distance of 10 Mpc).

#### 4.5 Covariance spectra

We extracted the covariance spectrum (see Uttley et al. 2014) from the EPIC-pn data in the frequency range  $(0.7\text{--}1.6) \times 10^{-4} \text{ Hz}$ . The covariance spectrum measures the spectral behaviour of the

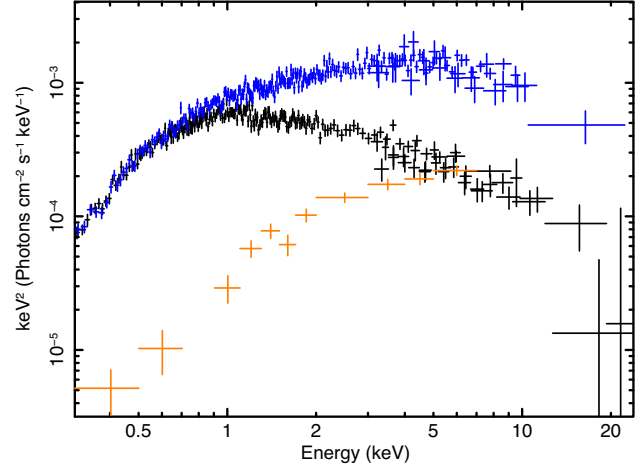
<sup>2</sup>The radial dependence of the disc temperature of the DISKPBB goes as  $r^{-p}$ , with  $p = 0.75$  for a standard disc and  $p = 0.5$  for a slim disc.

**Table 2.** Best-fitting spectral parameters. Errors are at 90 percent uncertainty for each parameter of interest.

Model	Component	2019 obs.		Previous obs.
		No flare	Flare	
TBABS	nH ( $10^{22}$ )		$0.11^{+0.01}_{-0.01}$	–
	kT <sub>seed</sub> (keV)		$0.13^{+0.01}_{-0.01}$	–
NTHCOMP	$\Gamma$	$2.47^{+0.04}_{-0.03}$	$1.75^{+0.02}_{-0.02}$	–
	E <sub>cut</sub>	$3.7^{+1.6}_{-0.8}$	$2.06^{+0.1}_{-0.1}$	–
	norm ( $10^{-4}$ )	$7.0^{+0.2}_{-0.2}$	$9.4^{+0.3}_{-0.2}$	–
	$\chi^2/dof$	1752.03/1804		–
TBABS	nH ( $10^{22}$ )		$0.138^{+0.009}_{-0.008}$	$0.16^{+0.03}_{-0.03}$
DISKBB	Tin (keV)		$0.28^{+0.02}_{-0.02}$	$0.20^{+0.03}_{-0.03}$
	norm		$8.3^{+3.0}_{-2.1}$	$20^{+24}_{-10}$
DISKPBB	Tin (keV)	$2.0^{+0.2}_{-0.1}$	$2.4^{+0.1}_{-0.1}$	$2.1^{+0.5}_{-0.4}$
	p	$0.500^{+0.004}_0$	$0.616^{+0.009}_{-0.009}$	$0.54^{+0.06}_{-0.03}$
	norm ( $10^{-3}$ )	$1.1^{+0.4}_{-0.3}$	$4.5^{+1.0}_{-0.9}$	$0.6^{+1.3}_{-0.4}$
	$\chi^2/dof$	1777.1/1803		492.3/465
TBABS	nH ( $10^{22}$ )		$0.15^{+0.01}_{-0.01}$	–
DISKBB	Tin (keV)		$0.26^{+0.01}_{-0.01}$	–
	norm		$13^{+6}_{-4}$	–
DISKPBB	Tin (keV)	$1.3^{+0.2}_{-0.1}$	$1.9^{+0.4}_{-0.3}$	–
	p	$0.5^{+0.016}_0$	$0.6^{+0.03}_{-0.01}$	–
	norm ( $10^{-3}$ )	$6.5^{+3.6}_{-2.5}$	$7.5^{+8.0}_{-3.0}$	–
	$\Gamma$	0.59 (frozen)		–
CUTOFFPL	E <sub>cut</sub>	7 (frozen)		–
	norm ( $10^{-5}$ )	$2.2^{+0.5}_{-0.5}$	$10^{+5}_{-7}$	–
	$\chi^2/dof$	1750.3/1801		–

short-term variability correlated with a given reference band. It allows to investigate the spectral components that are responsible of the variability. We compared the EPIC-pn covariance spectrum with those of the *persistent* and *flare* emission, in order to allow us to investigate the correlated spectral variability (Fig. 6). At a first glance, the spectral shape of the covariance spectrum is quite similar with the *flare* one.

We fitted the covariance spectrum with the best-fit model TBABS (DISKBB+DISKPBB+CUTOFFPL) of the *flare* spectrum. First, we multiplied it by a constant, which was left as the only free parameter, to account for an overall flux variation. We found that the model does not reproduce the covariance spectral shape correctly. Then, we removed the constant, and left the normalizations of the three spectral components (i.e. DISKBB, DISKPBB, and CUTOFFPL) free to vary independently. This approach provided a statistically acceptable result ( $\chi^2/dof = 14.62/9$ ): we found that the CUTOFFPL model contributes the most to describe the spectrum [normalization of  $(4.6 \pm 0.4) \times 10^{-5}$ ]. Instead, the DISKPBB normalization was almost two orders of magnitude lower [ $(1.7 \pm 1.1) \times 10^{-4}$ ] than the values found in either the *flare* or *persistent* spectra. Furthermore, the DISKBB normalization was consistent with zero and therefore it could be excluded by the fit. We note that letting free to vary also the DISKPBB temperature did not improve the quality of the fit. Instead, we found an improvement ( $\Delta\chi^2 \sim 4$  for 1 additional dof) by letting free

**Figure 6.** Covariance (the orange points), *flare* (the blue points) and *persistent* (the black points) spectra, unfolded through a power law of index 0. The covariance spectrum shows a spectral shape similar to the *flare* spectrum. Data have been rebinned for display purposes only.

to vary the photon index of the CUTOFFPL model. With this best fit, the normalization of the DISKPBB model became compatible with 0, while the CUTOFFPL photon index and normalization converged to  $0.79^{+0.08}_{-0.2}$  and  $(6.3^{+0.6}_{-1.4}) \times 10^{-5}$ , respectively. As a final step, we removed also the DISKPBB component and left free to vary also the cut-off energy of the CUTOFFPL model. The best fit is highly satisfactory ( $\chi^2/dof = 8.24/8$ ), and we obtained  $\Gamma = 0.4 \pm 0.4$ ,  $E_{cut} = 3.6^{+3.6}_{-1.3}$  keV, and Norm =  $(6.5^{+0.9}_{-0.8}) \times 10^{-5}$ . These results indicate that the correlated variability was mainly driven by the CUTOFFPL component.

#### 4.6 RGS spectra

The primary goal of the RGS is to resolve and constrain the properties of narrow features that are detected with higher statistics (albeit at lower resolution) in the EPIC spectra in the soft (<2 keV) X-ray band. To be consistent with the extraction of the EPIC spectra, we extracted the first-order RGS spectra in a cross-dispersion region of width 1 arcmin, centred at the emission peak. We extracted the background spectra by selecting photons beyond the 98 per cent of the source point spread function, and we checked for consistency by comparing the resulting spectrum with the background spectra from blank field data. We stacked the RGS 1 and 2 spectra for plotting purposes with the RGSCOMBINE task. The time-average stacked RGS spectrum is shown in Fig. 7 along with the EPIC-pn spectrum. In order to search for any changes in the narrow spectral features during the source flare events, we extracted flare-resolved spectra from the RGS 1 and 2 by running the *rgsproc* task and using the GTIs that were used to produce the *flare* EPIC-pn spectrum.

The RGS spectra cover a limited energy band, which means that an additional broad-band spectrum has to be used in order to constrain the continuum shape, and to avoid systematics in the search for narrow spectral features. Therefore, we simultaneously fitted the RGS and pn spectra because the latter, amongst the *XMM-Newton* detectors, features the highest effective area all the way up to 10 keV. Here, we do not use the MOS 1 and 2 spectra for two reasons: (1) their effective area in the Fe–K band is significantly lower than the pn’s; (2) their high count rate in the soft band of the RGS (together with that of pn) would wash away the statistical weight from the RGS data, which makes hard to detect the features.



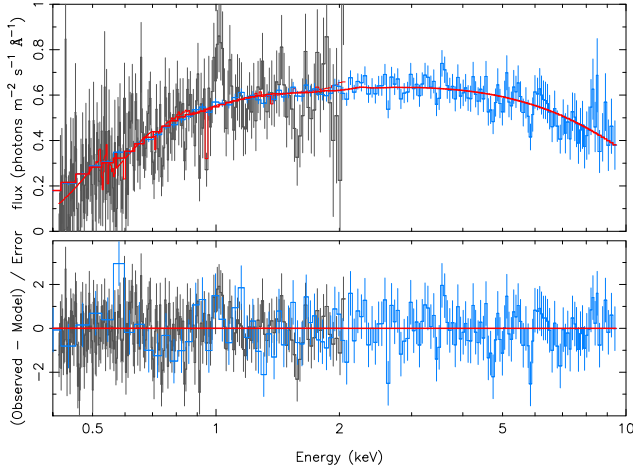


**Figure 7.** *XMM-Newton* EPIC-pn (light blue) and RGS (dark grey) time-averaged spectra of X7 from the 2019 *XMM-Newton* observation (top panel). The red solid lines show the best-fit SPEX Comptonization continuum model. The bottom panel shows the corresponding residuals. The spectra have been rebinned for displaying purposes.

The simultaneous spectral analysis of the RGS and EPIC-pn data is performed using a minimal binning of one third of the line spread function in order to avoid a loss in spectral resolution. We used the SPEX software<sup>3</sup> (Kaastra, Mewe & Nieuwenhuijzen 1996) to carry out the spectral analysis, and we adopted the C-statistics (Cash 1979). We analysed the EPIC-pn spectrum between 0.3–10 keV and the RGS 1 and 2 spectra between 6 and 30 Å (~0.4–2 keV). While in principle the RGS spectra could extend down to 0.3 keV, we note that the background already dominates the X-ray emission below 0.5 keV.

As shown in Section 4.4 and in Table 2, a simple model consisting of an absorbed Comptonization component is able to reproduce both the *XMM-Newton* and *NuSTAR* spectra. Therefore, as we have used NTHCOMP in the XSPEC modelling, we use the corresponding COMT model in SPEX to describe the EPIC-pn and RGS spectra in both the time-averaged and flared-resolved approaches. Of course, the SPEX/COMT parameters are consistent within the uncertainties with those estimated for XSPEC/NTHCOMP. Unsurprisingly, the column density of the absorbing interstellar medium is also consistent with the values derived within XSPEC. The SPEX spectral continuum model for the averaged spectra and the corresponding residuals are shown in Fig. 7.

There are positive residuals in both RGS and pn at 1 keV and negative residuals on both edges of the energy range, which are similar to those found in many other ULX spectra from *XMM-Newton*, *Chandra*, and *Suzaku*. Such residuals have been interpreted as the evidence for the presence of winds (see e.g. Middleton et al. 2015b), and they are often resolved with RGS in rest-frame emission and blue-shifted absorption lines from ionized atomic species (Pinto et al. 2016; Kosec et al. 2018). We performed a Gaussian line scan over the whole *XMM-Newton* energy band in order to search for the energy centroids of the strongest features. We decided to keep the pn spectrum in the range 0.3–2 keV (avoiding to fit the RGS spectrum alone), in order to minimize systematic effects of the RGS instrumental features, although EPIC spectra have a lower spectral resolution. In fact, Kosec et al. (2018) have shown that exposures

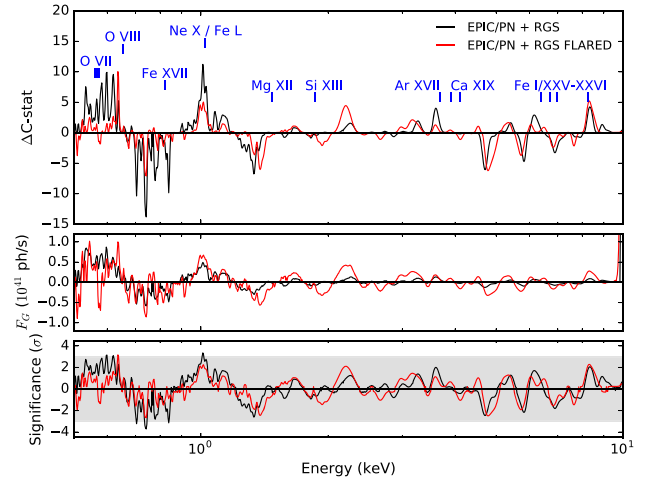


**Figure 8.** Gaussian line scan performed on the *XMM-Newton* RGS and pn time-averaged (black) and flared-resolved (red) spectra of the 2019 *XMM-Newton* observation. The fit improvement or  $\Delta C$ -stat (top) and the single trial significance (bottom) have been multiplied by the sign of the Gaussian normalization (middle panel) to distinguish between emission (positive flux) and absorption (negative flux) lines. The rest-frame energies of the strongest K and L transitions in the X-ray band are labelled.

larger than 120 ks of bright ULXs are typically required to detect significant features in the RGS spectra alone.

Following the approach used in Pinto et al. (2016), we searched for narrow spectral features by scanning the RGS and the pn spectra with Gaussian lines, adopting a logarithmic energy grid with energy steps comparable to the RGS and pn resolving power in the 0.5–2 and 2–10 keV energy ranges, respectively. We adopted a line width of 500 km s<sup>-1</sup> FWHM (i.e. comparable with the RGS spectral resolution). At each energy bin, we express the single trial significance as the square root of the  $\Delta C$ -stat. This provides the maximum significance for each line.

In Fig. 8, we show the results of the line scan obtained for the time-averaged (black) and the flare-resolved (red) RGS+pn spectra. The presence of an emission feature at 1 keV (likely due to Ne X or Fe L ions) is found, with a possible higher flux during the flaring state. A similar behaviour is seen for the emission-like features around 0.6 keV, which may be due to O VIII. A cluster of absorption features between 0.7 and 0.8 keV are found and, in previous works, were attributed to blue-shifted O VII–VIII absorption lines. The ions responsible for the 1 keV emission might be the cause of the putative absorption feature seen around 1.6 keV, albeit requiring blueshift.

In order to constrain better the line significance, we performed line scan of 1000 EPIC-pn + RGS spectra, simulated with a Monte Carlo approach by adopting the best-fitting continuum model of the average spectrum, and we searched for fake lines in the same way as we did for the observed EPIC-pn+RGS spectrum. To address the significance of the three main features, we checked the probability of having two (fake) spectral features yielding  $\Delta C$ -stat (DC) equal to or above that of the two emission lines found in the real data. This gave a probability of 99 per cent (i.e.  $\sim 2.6\sigma$ ), and this was determined by combining the  $p$  values of the individual probabilities. A comparable confidence level was obtained by searching simulated spectra for at least 1 spectral feature with DC stronger than that of our most relevant absorption feature at 0.74 keV. The probability of finding individual fake features around 0.5–0.6 and 0.9–1.1 keV with DC equal or above 10 was even smaller. We therefore believe the real significance of the observed lines to be between  $2.6\sigma$  and  $3.0\sigma$  each.

<sup>3</sup><http://www.sron.nl/spex>

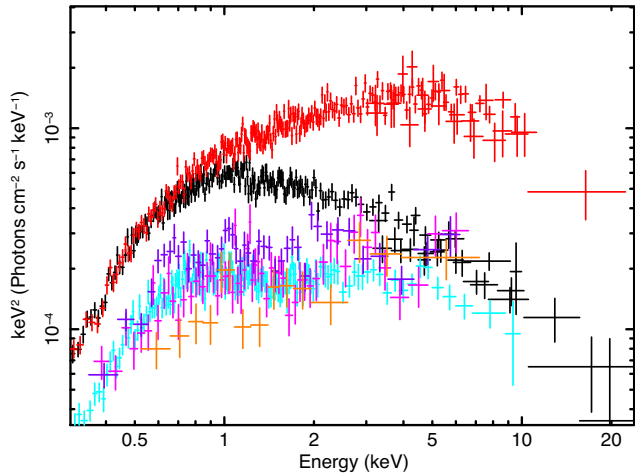


**Figure 9.** Spectra of all the available high-quality X-ray data unfolded through a power law of photon-index 0. The black and red point refer to the *flare* and *persistent* spectra of the 2019 *XMM-Newton*/EPIC-pn and *NuSTAR* observations; cyan points indicate the 2006 *XMM-Newton*/EPIC-pn spectrum; the fuchsia, violet, and orange points show the *Chandra* spectra in Obs.ID: 2026, 2027, and 2686, respectively. Spectra have been rebinned for display purposes only.

Ideally, one should perform an ad hoc, time-consuming, physical models automatic grid search (e.g. Kosec et al. 2018; Pinto et al. 2020), but this is not the focus of this work and it will be left for a forthcoming paper.

## 5 ARCHIVAL CHANDRA AND XMM-NEWTON OBSERVATIONS

Finally, we analysed the source spectra of the previous *XMM-Newton* and *Chandra* observations. As a first step, we unfolded the spectra with a power law of photon index 0 and we compared them with the 2019 *persistent* and *flare* spectra (Fig. 9). We found that the 2003 *XMM-Newton* and *Chandra* spectra are all compatible, with only subtle changes at soft energies, and in general consistent at energies above  $\sim 5$  keV with the 2019 *persistent* spectrum.

We fitted the 2013 *XMM-Newton* and *Chandra* spectra simultaneously, adopting an absorbed DISKBB+DISKPB model and a common absorption column. The fit gave a quite reasonable description of the data ( $\chi^2_{\nu} = 492.3/465$ ), with a mean 0.3–10 keV absorbed flux of  $\sim 8 \times 10^{-13}$  erg cm $^{-2}$  s $^{-1}$ , corresponding to a luminosity of  $9.5 \times 10^{39}$  erg s $^{-1}$ . Results are reported in Table 2.

## 6 DISCUSSION

We present the first long-term light curve of X7, using all the available *Swift*/XRT, *XMM-Newton*, *Chandra*, and *NuSTAR* observations taken between 2001 and 2020. Because of new high-quality *XMM-Newton* and *NuSTAR* observations taken in 2019, we could investigate the source short-term temporal and spectral variability, and we characterized them in great detail.

### 6.1 Flaring activity

The source long-term flux evolution shows that X7 appears to be persistent (i.e. it is detected in each observation) and exhibits a flux variability of up to a factor of  $\sim 6$  (from a luminosity of  $\sim 7 \times 10^{39}$  to  $\sim 4 \times 10^{40}$  erg s $^{-1}$ , assuming a reference distance

of 10 Mpc) over about 20 yr of observations. We also report on a possible (super)orbital variability with period of  $\sim 190$  d, to be confirmed by new continuous monitoring of the source. We note that superorbital variabilities are seen in several ULXs with periods of tens to a few hundreds days (e.g. Walton et al. 2016a; Fürst et al. 2018; Weng & Feng 2018; Vasilopoulos et al. 2020) therefore the X7 periodicity would be in line with those. In addition, we remark that the possible X7 periodicity is better seen at high energies, for which disc precession effect may be stronger.

On ks time-scales, X7 is even more variable and shows clear flaring activity, which we observed for the first time in our most recent observations (2019). The flaring activity manifests itself only when the source is at its highest observed luminosities. At the peak of the flares, the luminosity was a factor of  $\approx 3$  higher than the pre-flare luminosity, which implies that the maximum variability can span almost an order of magnitude. About six flares were identified in the 2019 *XMM-Newton* and *NuSTAR* observations, with a typical duration of  $\sim 5$ –10 ks, and no obvious periodic or quasi-periodic pattern. Based on our data, flares appear to happen only at high fluxes (or luminosities higher than  $2.5 \times 10^{40}$  erg s $^{-1}$ ), and are quite rare. We could find flares only in two observations over a total of more than 50: no clear flares were observed in the *Swift*/XRT, *Chandra*, and 2003 *XMM-Newton* observations, although the number of *Swift*/XRT observations is large, we note that their exposure times are typically  $\sim 2$  ks therefore shorter than the common flare duration, which prevents or strongly limits the detection of possible flares. Indeed, the scatter in flux of X7 in the *Swift*/XRT observations is quite wide (a factor of  $\sim 6$ ) and we cannot exclude that random bits of the flares are actually seen during the highest *Swift*/XRT luminosities [ $\sim (2-3) \times 10^{40}$  erg s $^{-1}$ ]. In particular, during the *Swift*/XRT observation 00032249048, we found that the source experienced a flux variability up to a factor of 3 suggesting a possible, partially seen, flare.

Furthermore, a prolonged high-flux phase, which lasted about 15 ks, was identified at the end of the 2019 *XMM-Newton* observation, and whose nature is unclear. During this time interval, the average flux was consistent with that observed at the peak of the flares, and shallow dip-like features can be observed. However, no significant spectral variations occur during the ‘dips’, which indicates that most likely such features are accretion-driven, rather than, e.g. induced by temporal increases in the local absorption, unless it is highly ionized (which would indeed be achromatic). It is also possible that a series of unresolved flares mimics the presence of dips. This possibility might be supported by the similar flux values reached during the isolated flares, and the high-flux phase. This behaviour is reminiscent of one of the many variability classes of the BH binary GRS 1915+105 – class  $\kappa$  (Belloni et al. 2000) – which is characterized by isolated events, followed by trains of flares with short recurrence times. Such a behaviour, if observed in a significantly fainter source (which means that data quality will have a low count statistics), would be comparable with what we observed in the latest *XMM-Newton* observation of X7.

Flaring activity is not common in ULXs, and it was observed in the sources M51 ULX-7 (Earnshaw et al. 2016), NGC 253 X-1 (Barnard 2010), NGC 6946 ULX-3 (Earnshaw et al. 2019), NGC 1313 X-1 (Walton et al. 2020), and NGC 7456 ULX1 (Pintore et al. 2020). In none of them a (quasi-)periodicity of the flare recurrency was identified, as opposed to the quasi-periodic heartbeat of the ULX 4XMM J111816.0-324910 in the galaxy NGC 3621 (Motta et al. 2020). This may indicate that the flares in ULXs cannot be explained with only one mechanisms and, furthermore, whatever process that generates flares might or not generate periodic events. In fact, generally speaking the presence of flares does not appear to

be clearly related to a specific spectral state or luminosity level (the range spanned by these source is very broad), although it seems that many ULXs preferentially flare during their brightest states. If we consider the spectral state of a given source, we remark they are quite different, which suggests that the high short-term activity can appear in both *soft ultraluminous*, *broadened disc*, and *hard ultraluminous* states (where we adopted the spectral classification of Sutton, Roberts & Middleton 2013).

## 6.2 Spectral evolution

The spectral properties of X7 varied over the years, passing through a *soft-ultraluminous* state, with luminosities  $< 3 \times 10^{40} \text{ erg s}^{-1}$ , to a *hard-ultraluminous* state characterized by flares. X7 is one of the best example of a ULX switching across two extreme ULX states. The general behaviour of the ULX population shows that sources can transit from *soft-ultraluminous* to *broadened disc* states, or from *hard-ultraluminous* to *broadened disc* states, or vice versa, but it is not often observed the transition from a *soft-ultraluminous* to a *hard-ultraluminous* state (see e.g. the hardness–intensity/colour–colour diagrams; Sutton et al. 2013; Pintore et al. 2017). We have shown that the X7 spectra can be modelled with the combination of at least two thermal components, i.e. a standard multicolour blackbody disc (DISKBB) at low energies and a ‘modified’ one (DISKPBB) at high energies. Such phenomenological model was proven to be a good representation of the spectra of a large sample of ULXs containing both PULXs and sources with compact objects of unknown nature (e.g. Stobbart, Roberts & Wilms 2006; Pintore et al. 2015; Koliopanos et al. 2017; Walton et al. 2020). Based on our results it appears that, in X7, the behaviour of the two disc components correlates with the luminosity (see Fig. 5).

In particular, *at low luminosity*, the soft DISKBB component, which describes a standard Shakura–Sunyaev disc (Shakura & Sunyaev 1973), shows a temperature of  $\sim 0.2 \text{ keV}$  and an inner radius of  $4.5_{-1.3}^{+2.2} \times 10^3 \sqrt{1/\cos(i)}$  km (where  $i$  is the inclination angle of the system). The hard disc component, i.e. the DISKPBB, is likely to be ascribed to an advection-dominated accretion flow (as suggested by the  $p$  parameter, which assumes a value of  $\sim 0.5$ ), and its apparent temperature converged at  $\sim 2 \text{ keV}$ . Such a component is responsible for about the 70 per cent of the 0.3–10 keV emission, therefore it dominates the X-ray flux in this band. We constrained its apparent inner disc radius at  $25_{-10}^{+19} \times \sqrt{1/\cos(i)}$  km. On the one hand, the small size of the radius of the hard disc component rules-out the presence of a disc around an IMBH. We stress that, should this radius be the innermost stable circular orbit ( $R_{\text{isco}} = 6 GM/c^2$ , for a non-rotating compact object), the mass of the compact object would be  $\sim 1.4\text{--}4 M_{\odot}$  and hence compatible with either a NS or a light BH. We note that for both disc components, the radii are estimated without taking into account any colour correction factor or boundary conditions: if we adopt a colour correction factor of  $f_{\text{col}} = 1.7$  (e.g. Shimura & Takahara 1995) and a boundary condition factor  $\xi = 0.4$  (e.g. Kubota et al. 1998), the radius estimates can be obtained from  $R_{\text{in}} = \sqrt{K (\xi D f_{\text{col}}^2)^2 / \cos(i)}$  (where  $K$  is the disc normalization,  $D$  is the source distance): for the disc normalization values found in our spectral analysis, we calculated  $R_{\text{inDISKBB}} \sim 3000$  and  $R_{\text{inDISKPBB}} \sim 16$  km, further strengthen that the compact object is likely of stellar origin (although its mass cannot be constrained yet in an obvious way).

*At higher luminosity*, in epochs of the light curve far from the flares, the spectra present an increase of the flux for energies below  $\sim 5 \text{ keV}$ , while at higher energies the source flux did not change significantly with respect to the lower flux spectra. A similar behaviour was

identified in NGC 1313 X-1 and Holmberg IX X-1 (Walton et al. 2016b, 2020; Gúrpide et al. 2021), which are both relatively hard sources and both present a high-energy tail that dominates the spectrum above 10 keV. The origin of such a stable high energy tail has been explained in a super-Eddington accretion scenario, where the matter in the accretion flow is removed in a disc-fed outflow and this dampens most of the accretion rate variability at large radii, which leaves only low variability in the inner regions (Middleton et al. 2015a) that therefore appear more stable. At super-Eddington rates, the outflows are expected to form a funnel, which is responsible for the geometric beaming of the high energy emission. Such a scenario is one of the most likely explanation of the properties and behaviour of the Galactic X-ray binary SS 433, which is believed to be an edge-on Galactic ULX (Begelman, King & Pringle 2006). When the accretion rate increases further, the outflow opening angle can narrow (e.g. King 2009) even further, thus exacerbating the geometrical beaming of the high energy emission. Hence, in the sources with a hard-tail, the stability of the high-energy component may indicate that, even though the flux is rising (i.e. the accretion rate is increasing), the emission of the wind is increasing as well, but the changes in accretion rate are not prominent enough to significantly affect the geometrical beaming. Alternatively, the increase of the accretion rate does not affect the aperture of the cone of the outflows, but rather it only increases the size of the apparent outflow emitting radius, i.e. the smallest disc radius at which outflows are ejected. In this last case, the beaming may present a radial dependence, which implies that only the emission produced within a characteristic radius can be beamed (see e.g. Lasota et al. 2016; Walton et al. 2020). In the case of X7, at least the first interpretation we described (i.e. a not changing geometrical beaming) may hold as the flux and spectral variability is mainly observed at low-middle energies, where the contribution of the outflow emission is thought to be dominant.

Instead, during the flares and at the highest source fluxes, X7 undergoes an abrupt spectral change with respect to the pre-flare state (see Fig. 2). While the flare and pre-flare spectra are consistent at energies below 1 keV, a clear increase in flux is observed above 1 keV during the flares. In addition, a third non-thermal spectral components may pop-up at energies  $> 10 \text{ keV}$ . Such a component is being detected in an increasing number of sources when high-quality and broad-band data are available, and it is generally well modelled by a cut-off power-law. Remarkably, this component tends to be stronger in PULXs (see e.g. Walton et al. 2018) and for this reason it is generally interpreted as the presence of the accretion column on the top of the NS in these sources. Our spectral modeling during the highest flux epochs and during the flares shows that the softer thermal component does not vary appreciably in flux with respect to the pre-flare epochs. This has a temperature of  $\sim 0.2 \text{ keV}$  and its corresponding emitting radius is  $3.6_{-0.6}^{+0.8} \times 10^3 \times \sqrt{1/\cos(i)}$  km, consistent with the value derived for the same component when observed at lower flux epochs. In contrast, the hard disc component shows an apparent inner radius of  $(80_{-20}^{+40} \times \sqrt{1/\cos(i)}) \text{ km}$ , which is larger than what we found at lower fluxes, although its temperature does not change significantly.

Based on our finding, and on the comparison between our results and what has been observed in other ULXs, we argue that each spectral component can be interpreted in the context of a super-Eddington accretion scenario, where the accretion flow is formed by an outer disc; an advection-dominated disc (or thick disc), which is covered by an optically thick outflow; and an inner accretion flow. The inner accretion flow could be a ‘naked’ (i.e. without outflows) advection-dominated disc or an optically thick corona covering the inner disc regions and the compact object. Alternatively it may be



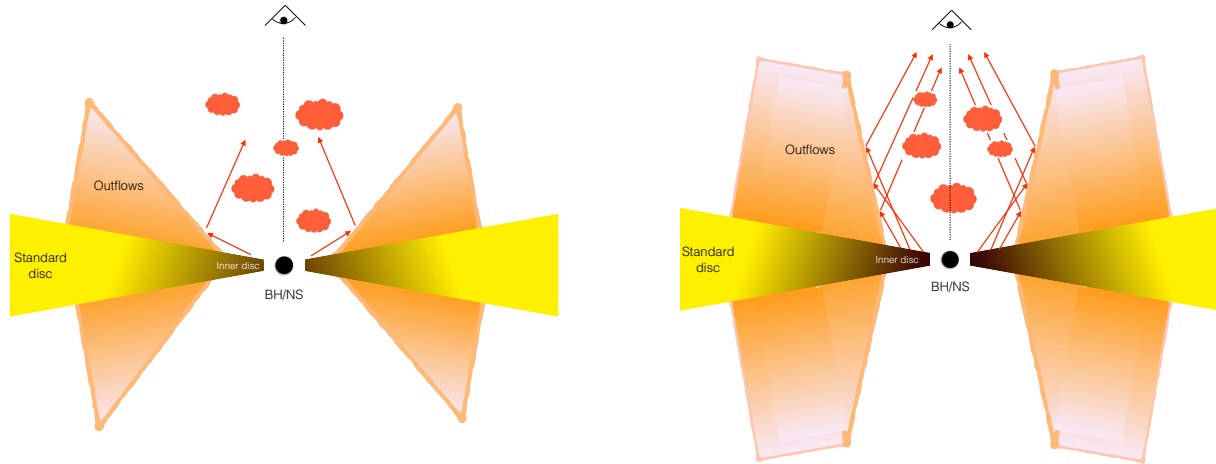


**Figure 10.** Schematic representation of the accretion flow in X7, where we assume that the accretion is super-Eddington and the LoS is close to be face-on. *Left:* The sketch shows the low flux state, in which a geometrical beaming of the inner regions is produced by the wall of the outflows. A standard accretion disc is expected in the outer regions. Optically thin turbulences are inside the wind cone producing the observed absorption and emission features. *Right:* the accretion flow during the flares and the high flux epochs. An enhancement of the accretion rate returns a narrowing of the wind cone opening angle, increasing the beaming of the inner regions.

an optically thick boundary layer, should the compact object be an NS (see Mushtukov et al. 2015). We associate (i) the outer disc to the softer thermal component (DISKBB), which we expect to be in a standard regime (e.g. Shakura & Sunyaev 1973); (ii) the thick-disc/outflows to the high-energy DISKPB component; and (iii) the cut-off power-law to the inner disc or the boundary layer.

### 6.3 Evidences of outflows

According to our spectral analysis, the soft disc component does not vary significantly in neither flux or temperature, which suggests that the size of its inner radius was constant even though the total flux increased by about an order of magnitude. Because the data points are limited, we cannot claim any relation between the disc luminosity and its temperature. More high-quality observations at different fluxes will allow us to investigate if the outer disc properties can be firmly associated with a standard disc. Similar considerations can be done for the high-energy disc component, which we associated with the photosphere of outflows ejected by the accretion disc. An analysis of the high quality 2019 *XMM-Newton/RGS* spectra allowed us to detect blue-shifted absorption and emission features. The former are probably due to O VII–VIII, while the latter are likely associated with Ne X or Fe L transitions. The significance of such spectral features is limited by the short exposure we had to employ, but the strict similarity with features reported in previous work (see e.g. Pinto et al. 2016; Pinto et al. 2017; Kosec et al. 2018; Wang, Soria & Wang 2019) provides support for the presence of optically thin plasma and, likely, optically thick winds in X7. Given the likely presence of the winds, we note that the DISKPB is a phenomenological model that can only mimic the more complex spectral emission of the outflows. We found that the flux evolution of this component is consistent with the photosphere of a wind increasing in size (the apparent emitting radius evolved from  $\sim 25$  to  $\sim 80$  km) and decreasing in temperature because of the expansion. Our results indicate that the existence of outflows in X7 strengthens even more the compact object stellar origin, which we claimed to be likely an NS or a stellar mass BH. Indeed, should the compact object being an IMBH, for the observed luminosity we would expect sub-Eddington or Eddington accretion

rates, for which we do not expect powerful optically thick winds, nor an emission that spectrally bends below 10 keV.

Our results seem to indicate that X7 is seen from a small inclination angle, i.e. our line of sight intersects the cone produced by the wall of the optically thick outflow. In this scenario, the flares originate from a large increment of the accretion rate, which is able to significantly modify the geometrical structure of the outflows, in particular closing the aperture angle of the wind cone, favouring a stronger geometrical beaming of the high-energy inner emission of the accretion flow. This results in a larger high energy flux, and thus in an hardening of the spectra during the flaring activity (see the sketch in Fig. 10).

### 6.4 Short-term temporal properties

The lags discovered in X7 can be explained in the super-Eddington framework as well. The hard lag is such that the high energy emission lags the soft one by  $\sim 300$ s, on time-scales of  $\sim 10^{-4}$  Hz. Hard lags are observed at low frequencies in a variety of Galactic X-ray binaries (Miyamoto et al. 1988; Arévalo & Uttley 2006) and active galactic nuclei (e.g. De Marco et al. 2013; Alston, Vaughan & Uttley 2013; Kara et al. 2014, 2016; Uttley et al. 2014). Hard lags are commonly believed to be caused by the inward propagation of fluctuations in the accretion flow, for which the outer regions of the flow (responsible for the soft photons’ emission) respond earlier than the inner regions where high-energy photons are produced (Kotov, Churazov & Gilfanov 2001; Arévalo & Uttley 2006). X7 is the first ULX where low-frequency hard lags have been observed, with an average value of  $334 \pm 89$ s. We can explain such lags in terms of the inward propagation of mass accretion rate fluctuations, which is also responsible for the flares.

An alternative scenario may instead relate the low-frequency range of the lag to the temporal length between the flares: in such a case, a scattering of soft photons from a very extended optically thin corona or a jet may be likely. The corona can be supported by the RGS spectroscopic analysis, which showed the existence of emission possibly produced in an optically thin plasma. Should the hard lag simply be the crossing time of the soft photons into a hot and optically thin medium, it implies a size of  $\sim 10^{13}$  cm, which may be too large



and unfeasible. Hence, the inward propagating fluctuations remain the best explanation for the source hard lag.

In addition, we also remark the existence of a weak soft lag at frequencies  $\sim(2 - 4) \times 10^{-4}$  Hz with a weighted average value of  $395 \pm 167$  s. Soft lags were reported for the sources NGC 55 ULX-1 (Pinto et al. 2017), NGC 1313 X-1 (Kara et al. 2020), and NGC 5408 X-1 (De Marco et al. 2013), with magnitudes from tens to thousands of ks. Soft lags are commonly associated with delays due to the crossing time and down-scattering of hard photons passing through the optically thick outflows. The interpretation of the soft lags in these sources then points towards a quite high inclination angle of the systems. However, the phenomenology of X7 seems instead to point towards a quite low inclination of the system. Should the soft lag in X7 be real, this would be in line with the magnitudes observed in the other ULXs, but it may be interpreted as reflection of the hard photons from a lower temperature region. Assuming that the Compton scattering is the dominant process, the radius of the scattering region can be estimated as  $R = \sqrt{\frac{ct}{\sigma_T n_e}}$ , where  $c$  is the speed of light,  $t$  is the soft lag in seconds,  $\sigma_T$  is the Thomson cross-scattering, and  $n_e$  is the electron density. Assuming a disc/wind electron density of  $n_e \sim 10^{20} \text{ cm}^{-3}$  (e.g. Shakura & Sunyaev 1973; Takeuchi, Ohsuga & Mineshige 2013) and a single scattering, the size of the scattering medium would then be  $<10^7 - 10^8$  cm, i.e. larger than the characteristic inner disc radii estimated from the spectral analysis, and instead consistent with the outer regions of the accretion flow or with the base of the outflow. We note that the estimated size could be smaller if we allow for multiscatterings of the hard photons into the medium.

Finally, although we analysed the highest quality available data of the source, which shed light on the geometry and structure of the accretion flow, the exact nature of the compact object in X7 remains dubious. The timing analysis did not provide any strong indication on the existence of pulsations, but only some hints of pulsations when orbital corrections are applied, the statistical significance of which is very low. More high-quality data are needed to confirm or refute such a tentative pulsation detection. The large flux variation on long time-scale, the hard spectra during the flares and the small size of the inner disc during the low flux epochs can favour X7 hosting an NS. We note that, should the compact object be a magnetic NS able to truncate the inner accretion flow at radii of tens of km, as suggested by our spectral analysis, by assuming a beaming factor of 0.1, we derive a dipolar magnetic field of magnitude  $10^{10} - 10^{11}$  G.

## 7 CONCLUSIONS

We analysed all the available X-ray observations of the ULX X7 taken with *XMM-Newton*, *NuSTAR*, *Chandra*, and *Swift/XRT*. Its long-term variability features changes in flux of up to an order of magnitude, with extreme luminosity reaching an observed maximum of  $\sim 6 \times 10^{40} \text{ erg s}^{-1}$  during flare activity. The spectral analysis of the high quality *XMM-Newton* and *NuSTAR* observations allowed us to characterize the properties of the source, which we modelled with two thermal disc-like components. We interpret the source spectral and temporal evolution within the framework of super-Eddington accretion and we associated the soft disc component to an outer, standard razor-thin accretion disc, while the high-energy disc to the photosphere of a powerful optically thick outflow above the disc. Confirmation on the existence of a wind comes from the detection of blue-shifted absorption and emission features in the RGS data, which indicate also the presence of an optically thin plasma. We also note that during the flare, a third spectral component could be exhibited by

X7. Comparing it with the ones observed in a number of ULXs, we may associate it to either an accretion column density if the compact object is an NS or a boundary layer/optically thick corona in case of a BH accretor. We propose that the source evolution can be explained with variations of the accretion rate that can affect the geometrical cone of the outflow, enhancing the degree of beaming of the inner regions responsible for the high-energy emission.

## ACKNOWLEDGEMENTS

This work has been partially supported by the ASI-INAF agreements 2017-14-H.0.

## DATA AVAILABILITY

All of the data underlying this article are already publicly available from ESA's *XMM-Newton* Science Archive (<https://www.cosmos.esa.int/web/XMM-Newton/xsa>), NASA's HEASARC archive (<https://heasarc.gsfc.nasa.gov/>), and the *Chandra* Data Archive (<https://cxc.harvard.edu/cda/>).

## REFERENCES

- Alston W. N., Vaughan S., Uttley P., 2013, *MNRAS*, 435, 1511  
 Arévalo P., Uttley P., 2006, *MNRAS*, 367, 801  
 Bachetti M. et al., 2013, *ApJ*, 778, 163  
 Bachetti M. et al., 2014, *Nature*, 514, 202  
 Band D. L., 1997, *ApJ*, 486, 928  
 Barnard R., 2010, *MNRAS*, 404, 42  
 Begelman M. C., King A. R., Pringle J. E., 2006, *MNRAS*, 370, 399  
 Belloni T., Klein-Wolt M., Méndez M., van der Klis M., van Paradijs J., 2000, *A&A*, 355, 271  
 Brightman M. et al., 2018, *Nat. Astron.*, 2, 312  
 Carpano S., Haberl F., Maitra C., Vasilopoulos G., 2018, *MNRAS*, 476, L45  
 Cash W., 1979, *ApJ*, 228, 939  
 De Marco B., Ponti G., Miniutti G., Belloni T., Cappi M., Dadina M., Muñoz-Darias T., 2013, *MNRAS*, 436, 3782  
 den Herder J. W. et al., 2001, *A&A*, 365, L7  
 Earnshaw H. M. et al., 2016, *MNRAS*, 456, 3840  
 Earnshaw H. P., Roberts T. P., Sathyaprakash R., 2018, *MNRAS*, 476, 4272  
 Earnshaw H. P. et al., 2019, *ApJ*, 881, 38  
 Fürst F. et al., 2018, *A&A*, 616, A186  
 Gúrpide A., Godet O., Koliopoulos F., Webb N., Olive J.-F., 2021, *A&A*, preprint ([arXiv:2102.11159](https://arxiv.org/abs/2102.11159))  
 Heil L. M., Vaughan S., 2010, *MNRAS*, 405, L86  
 Israel G. L., Stella L., 1996, *ApJ*, 468, 369  
 Israel G. L., Belfiore A., Stella L., Esposito P. e. a., 2017, *Science*, 355, 817  
 Israel G. L., Papitto A., Esposito P., Stella L. e. a., 2017, *MNRAS*, 466, L48  
 Kaaret P., Feng H., Roberts T. P., 2017, *ARA&A*, 55, 303  
 Kaastra J. S., Mewe R., Nieuwenhuijzen H., 1996, in Yamashita K., Watanabe T., eds, *UV and X-ray Spectroscopy of Astrophysical and Laboratory Plasmas SPEX: A New Code For Spectral Analysis of X & UV Spectra*. p. 411  
 Kara E. et al., 2014, *MNRAS*, 445, 56  
 Kara E., Alston W. N., Fabian A. C., Cackett E. M., Uttley P., Reynolds C. S., Zoghbi A., 2016, *MNRAS*, 462, 511  
 Kara E. et al., 2020, *MNRAS*, 491, 5172  
 King A. R., 2009, *MNRAS*, 393, L41  
 King A., Lasota J.-P., 2020, *MNRAS*, 494, 3611  
 Koliopoulos F., Vasilopoulos G., Godet O., Bachetti M., Webb N. A., Barret D., 2017, *A&A*, 608, A47  
 Kosec P., Pinto C., Fabian A. C., Walton D. J., 2018, *MNRAS*, 473, 5680  
 Kosec P., Pinto C., Walton D. J., Fabian A. C., Bachetti M., Brightman M., Fürst F., Grefenstette B. W., 2018, *MNRAS*, 479, 3978  
 Kotov O., Churazov E., Gilfanov M., 2001, *MNRAS*, 327, 799

- Kubota A., Tanaka Y., Makishima K., Ueda Y., Dotani T., Inoue H., Yamaoka K., 1998, *PASJ*, 50, 667
- Lasota J. P., Vieira R. S. S., Sadowski A., Narayan R., Abramowicz M. A., 2016, *A&A*, 587, A13
- Middleton M. J., King A., 2017, *MNRAS*, 470, L69
- Middleton M. J., Heil L., Pintore F., Walton D. J., Roberts T. P., 2015a, *MNRAS*, 447, 3243
- Middleton M. J., Walton D. J., Fabian A., Roberts T. P., Heil L., Pinto C., Anderson G., Sutton A., 2015b, *MNRAS*, 454, 3134
- Middleton M. J., Brightman M., Pintore F., Bachetti M., Fabian A. C., Fürst F., Walton D. J., 2019, *MNRAS*, 486, 2
- Miyamoto S., Kitamoto S., Mitsuda K., Dotani T., 1988, *Nature*, 336, 450
- Motta S. E. et al., 2020, *ApJ*, 898, 174
- Mushtukov A. A., Suleimanov V. F., Tsygankov S. S., Poutanen J., 2015, *MNRAS*, 454, 2539
- Ohsuga K., Mineshige S., 2011, *ApJ*, 736, 2
- Peterson B. M., Wanders I., Horne K., Collier S., Alexander T., Kaspi S., Maoz D., 1998, *PASP*, 110, 660
- Pinto C., Middleton M. J., Fabian A. C., 2016, *Nature*, 533, 64
- Pinto C. et al., 2017, *MNRAS*, 468, 2865
- Pinto C. et al., 2020, *MNRAS*, 492, 4646
- Pintore F., Esposito P., Zampieri L., Motta S., Wolter A., 2015, *MNRAS*, 448, 1153
- Pintore F., Zampieri L., Stella L., Wolter A., Mereghetti S., Israel G. L., 2017, *ApJ*, 836, 113
- Pintore F. et al., 2020, *ApJ*, 890, 166
- Poutanen J., Lipunova G., Fabrika S., Butkevich A. G., Abolmasov P., 2007, *MNRAS*, 377, 1187
- Rodríguez Castillo G. A. et al., 2020, *ApJ*, 895, 60
- Sanders D. B., Mazzarella J. M., Kim D.-C., Surace J. A., Soifer B. T., 2003, *AJ*, 126, 1607
- Sathyaprakash R. et al., 2019, *MNRAS*, 488, L35
- Shakura N. I., Sunyaev R. A., 1973, *A&A*, 24, 337
- Shimura T., Takahara F., 1995, *ApJ*, 445, 780
- Sorce J. G., Tully R. B., Courtois H. M., Jarrett T. H., Neill J. D., Shaya E. J., 2014, *MNRAS*, 444, 527
- Soria R., Motch C., Read A. M., Stevens I. R., 2004, *A&A*, 423, 955
- Stobbart A.-M., Roberts T. P., Warwick R. S., 2004, *MNRAS*, 351, 1063
- Stobbart A.-M., Roberts T. P., Wilms J., 2006, *MNRAS*, 368, 397
- Sutton A. D., Roberts T. P., Middleton M. J., 2013, *MNRAS*, 435, 1758
- Swartz D. A., Soria R., Tennant A. F., Yukita M., 2011, *ApJ*, 741, 49
- Takeuchi S., Ohsuga K., Mineshige S., 2013, *PASJ*, 65, 88
- Takeuchi S., Ohsuga K., Mineshige S., 2014, *PASJ*, 66, 48
- Tsygankov S. S., Mushtukov A. A., Suleimanov V. F., Poutanen J., 2016, *MNRAS*, 457, 1101
- Tully R. B., Fisher J. R., 1988, *Catalog of Nearby Galaxies*. Cambridge Univ. Press, Cambridge, UK, p. 224
- Uttley P., Cackett E. M., Fabian A. C., Kara E., Wilkins D. R., 2014, *A&AR*, 22, 72
- Vasilopoulos G., Lander S. K., Koliopoulos F., Bailyn C. D., 2020, *MNRAS*, 491, 4949
- Walton D. J. et al., 2016a, *ApJ*, 827, L13
- Walton D. J. et al., 2016b, *ApJ*, 827, L13
- Walton D. J. et al., 2018, *ApJ*, 856, 128
- Walton D. J. et al., 2018, *MNRAS*, 473, 4360
- Walton D. J. et al., 2020, *MNRAS*, 494, 6012
- Wang C., Soria R., Wang J., 2019, *ApJ*, 883, 44
- Weng S.-S., Feng H., 2018, *ApJ*, 853, 115
- Zdziarski A. A., Johnson W. N., Magdziarz P., 1996, *MNRAS*, 283, 193

This paper has been typeset from a  $\text{\TeX}/\text{\LaTeX}$  file prepared by the author.